



A numerical study on mechanical behavior of jointed rock masses after tunnel excavation

Wanzhi Zhang¹ · Bangshu Xu¹ · Jie Mei¹ · Guangyao Yue¹ · Weihang Shi¹

Received: 24 November 2018 / Accepted: 25 April 2020 / Published online: 30 May 2020
© Saudi Society for Geosciences 2020

Abstract

The tunnel in jointed rock masses is prone to be overbroken and then gives rise to collapse, yet the failure modes of jointed rock masses are still poorly understood. This paper investigates anisotropic deformations and failure modes of tunnels in jointed rock masses. For this purpose, five series of numerical models are modeled for a severe tunnel overbreak occurring on the Panlongshan tunnel. The ubiquitous joint model is used to consider the shearing and tensioning effects of the bedding and joint structures. The factors affecting anisotropic deformation and failure of rock masses, such as bedding spacing (s), joint dip angles (θ), and joint spacing (d), are discussed. The results demonstrate that for the stratified rock masses (without joint), the maximum settlement around the tunnel is located at the roof, and the separation of “virtual blocks” along the bedding planes is a basic failure mode; for stratified rock masses containing joints, the maximum deformation surrounding the tunnel appears in the joint position, and failure happens through a combined rotation, sliding, and falling mechanism. Our study can also reveal that with the increase of the number of joints, the plastic zone at the joint positions has a developing tendency towards the deep part. The more complex the joint structures in jointed rock masses are, the more unstable rock masses are formed.

Keywords Jointed rock masses · Tunnel · Numerical analysis · Deformation · Failure mode

Introduction

Stratified rock masses mainly include sedimentary rocks, para-metamorphic rocks, and volcanic rocks with layered structure, which are distributed broadly over land, accounting for 66.7% of the land area (Wu 2016). This kind of rock

masses contains a large number of bedding planes, which are dominant structure planes resulted from differences in material composition, material color, particle size, and arrangement structure. Stratified rock masses are transversely isotropic, whose composition is basically the same in the direction of parallel bedding planes and show soft and hard multilayer in the direction of vertical bedding planes. It is more common, however, to encounter other joint fissures cutting through rock layers. For jointed rock masses, a great number of joints fundamentally change the performance of the rock masses, which have an obvious anisotropy on mechanical behaviors such as strength and deformation patterns (Lisjak et al. 2014; Zhang and Liu 2002). From the engineering point of view, Goodman presented that the nature of the joint network is as important and even decisive as the mineral composition (Goodman 1989). Thus, when a tunnel passes through jointed rock masses, failure mechanism and stability of surrounding rock masses have changed considerably with respect to those in the homogeneous rock masses (Wu et al. 2004; Huang and Zhang 2012; Stille and Palmstrom 2008; Zheng et al. 2011; Wang et al. 2018).

In China, with fast-growing demands for transportation facilities, underground roads and railways are being planned

Responsible Editor: Marco Barla

✉ Bangshu Xu
xubangshu@sdu.edu.cn

Wanzhi Zhang
zwwanzhi@163.com

Jie Mei
201513301@mail.sdu.edu.cn

Guangyao Yue
201744710@mail.sdu.edu.cn

Weihang Shi
201714560@mail.sdu.edu.cn

¹ Geotechnical and Structural Engineering Research Center, Qianfoshan Campus, Shandong University, No. 17923 Jingshi Road, Jinan 250061, Shandong Province, People's Republic of China

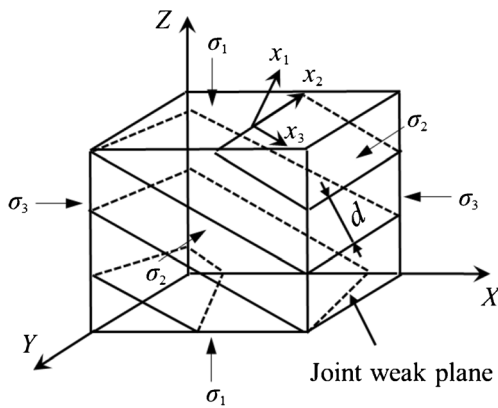
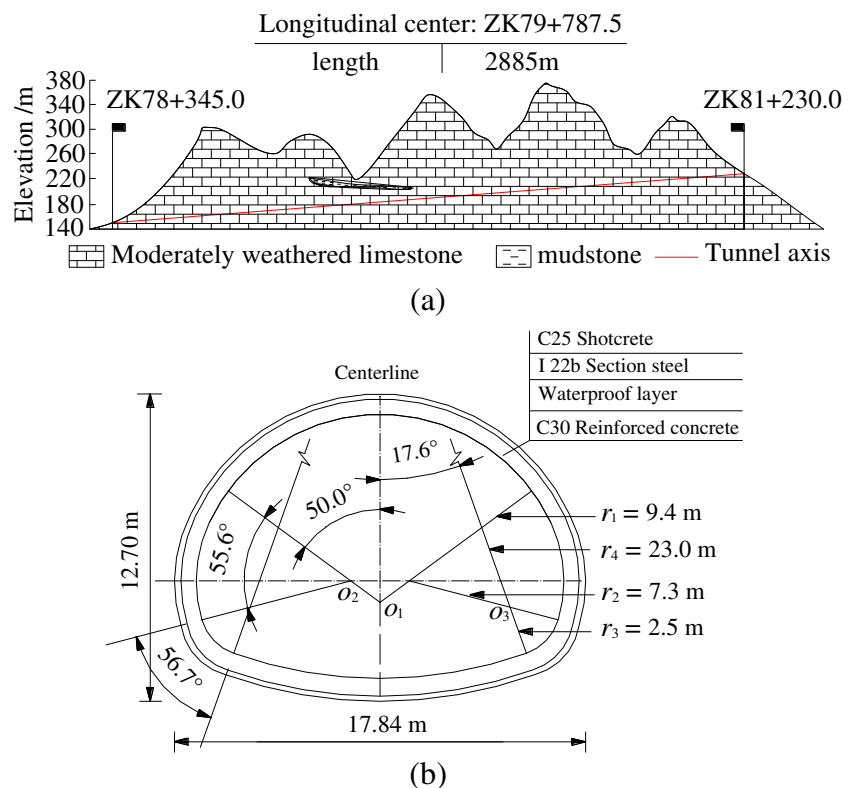


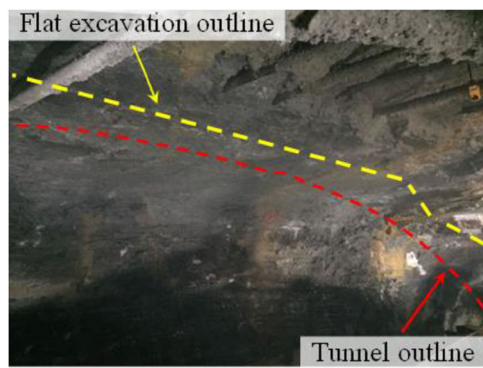
Fig. 1 Configuration of a three-dimensional rock mass with unit length in all sides and containing joint weak planes. A local coordinate for joint weak planes is defined

and constructed in the mountainous and urban areas, which are surrounded by a large number of jointed rock masses. Since dominant discontinuities may lead to a highly anisotropic behavior, it is necessary to systemically investigate failure mechanisms and stability problems of tunnels in jointed rock masses. Before the twentieth century, many scholars presented that the correlation between roof displacement and horizontal stress is higher than that with the vertical stress. The voussoir beam analogue is suitable for explaining the stability of the overlying rock masses in the underground excavation. The failure modes of layered roof mainly include buckling failure and rock shear failure (Evans 1941; Beer and Meek,

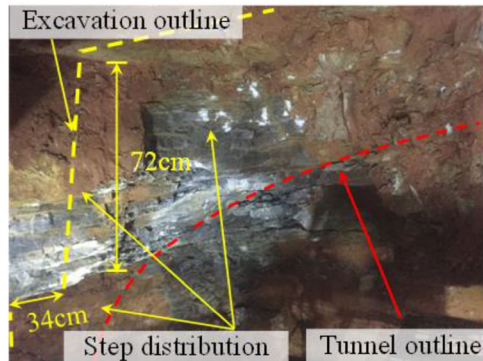
1982; Xiao and Ding 1993; Diederichs and Kaiser 1999; Yang et al. 2001; Huang et al. 2019). A general way to investigate the deformations and failure characteristics of tunnels in jointed rock masses is to carry out numerical simulation and physical experiment. Hao and Azzam investigated the influence of joint dips, joint shear strength, and joint locations on the plastic zones and displacements around underground openings in rock masses using UDEC (Hao and Azzam. 2005). Jiang et al. discussed the relationship between deformational behavior and dimension and orientation of joint sets based on numerical simulation of underground structure in jointed rock masses (Jiang et al. 2006). Jia and Tang studied the progressive failure process of tunnel in jointed rock masses applying numerical modeling (RFPA). Meanwhile, they proposed that both the dip angle of joints and the lateral pressure coefficient have significant impacts on the failure mode and displacement of tunnel (Jia and Tang 2008). Jeon et al. carried out scaled model tests to investigate the effect of a fault and grouting on the stability of a tunnel (Jeon et al. 2004). Liu et al. conducted a centrifugal model test to explore the destruction process of unsymmetrical loading tunnel in bedding rock masses (Liu et al. 2017). Some scholars had also systematically studied the effects of joint orientation on the cracking process in jointed rock masses by uniaxial and biaxial compression tests, and they concluded that failure modes are strongly affected by joint orientation (Chen et al. 2013; Bahaaddini et al. 2013; Han et al. 2018).

Fig. 2 a The longitudinal geological profile of the tunnel. b The standard section of the V rock

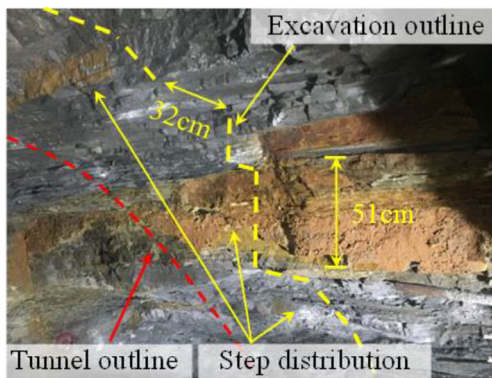




(a)



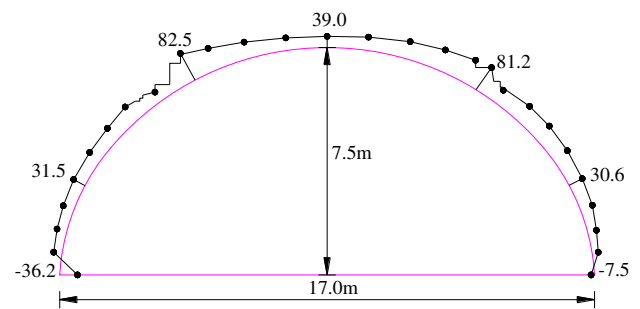
(b)



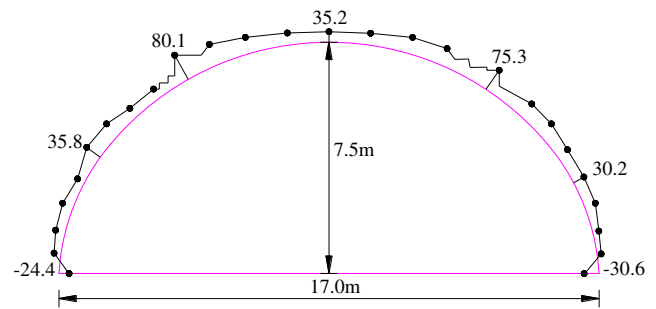
(c)

Fig. 3 Bedding and joint characteristics and failure modes of jointed rock masses after tunnel excavation. **a** Roof. **b** Left arch shoulder. **c** Right arch shoulder

For jointed rock masses, there are usually several joint sets in very different directions so that the rock mass is broken up into a blocky structure (Jaeger and Cook 1979). Some model tests and numerical results have shown that the failure of tunnel roof is mainly caused by the falling of “virtual blocks” that refer to rock masses with large deformations after tunnel excavation (Prudencio and Jan 2007; Zhang et al. 2012). Song et al. used a three-dimensional statistical joint modeling technique to analyze the stability of rock blocks around a tunnel, and they concluded that the failure of rock blocks was easy to occur as the degree of scatter in joint orientation increased (Song et al. 2001).



(a)



(b)

— Designed tunnel outline — Measured excavation outline

Fig. 4 Overbreak of the tunnel test sections (unit: cm). **a** ZK80+250.4 cross section. **b** ZK80+246.5 cross section

Although the influences of the bedding and joint structures in jointed rock masses on the deformation and stability of underground structures have been studied, both analytically and experimentally, the common effect of the bedding and joint structures on the mechanical behavior and overbreak of tunnels is still far from being complete and satisfactory. In this paper, the anisotropic deformations, the sizes of failure zone, and the distributions of plastic zone induced by the bedding and joint structures in jointed rock masses surrounding a tunnel are explored by FLAC3D (Fast Lagrangian Analysis of Continua in Three-dimensions) (Itasca Consulting Group, Inc. 2012). Here, the bedding and joint planes are modeled by ubiquitous joint model that is an in-built constitutive model of FLAC3D. Finally, the factors affecting anisotropic deformation of rock masses during tunnel excavation, such as s , θ , and d , are discussed.

Model methodology

Deformation of jointed stratified rock masses

Figure 1 presents a rock mass with a unit volume containing a set of joint weak planes with a uniform dip angle. The stress conditions, σ_1 , σ_2 , and σ_3 , are illustrated in this figure. Assuming that the jointed rock mass is subjected to a uniform stress σ , when σ increases by $d\sigma$, the corresponding incremental

strain is $d\varepsilon$. As a discontinuous medium, the jointed rock mass is generally considered to be composed of intact rock blocks and joints (Yang et al. 2018). According to Wang et al.'s research (Wang and Huang 2009), the incremental strains can also be divided into two components: the intact rock deformation $d\varepsilon^I$ and deformations of joint weak planes $d\varepsilon^J$.

$$d\varepsilon = d\varepsilon^I + d\varepsilon^J \tag{1}$$

Before the applied load reaches the peak strength, $d\varepsilon^I$ can be expressed as follows:

$$d\varepsilon^I = \mathbf{C}^I d\sigma \tag{2}$$

where \mathbf{C}^I is the compliance matrix of intact rock.

In order to derive $d\varepsilon^J$, local deformation on joint weak plane $d\delta$ is considered first. As shown in Fig. 1, the tendency of joint weak plane is defined by Cartesian coordinate components which x_1 is the normal vector, x_2 is the orientation of strike, and x_3 is the third direction following the right-hand rule.

$$d\delta = \mathbf{DLB}d\sigma \tag{3}$$

where $\mathbf{D} = [\mathbf{D}_{ij}]$, \mathbf{D}_{ij} ($i, j = 1, 2, 3$) is the element of the compliance matrix associated with joint weak planes; \mathbf{L} is the transformation matrix which is composed of directional cosines between local coordinates (x_1, x_2 , and x_3) and global coordinates (X, Y , and Z); \mathbf{B} is a matrix representing the area projection of joint weak planes onto the $Y-Z$ plane, $Z-X$ plane, and $X-Y$ plane.

Global deformation du can be expressed through a further transformation as follows:

$$du = \mathbf{L}^T \mathbf{DLB} d\sigma \tag{4}$$

When further considering d , $d\varepsilon_i^J$ can be described by

$$d\varepsilon_i^J = \frac{du_i \cdot n_i}{d}, i = x, y, z \tag{5}$$

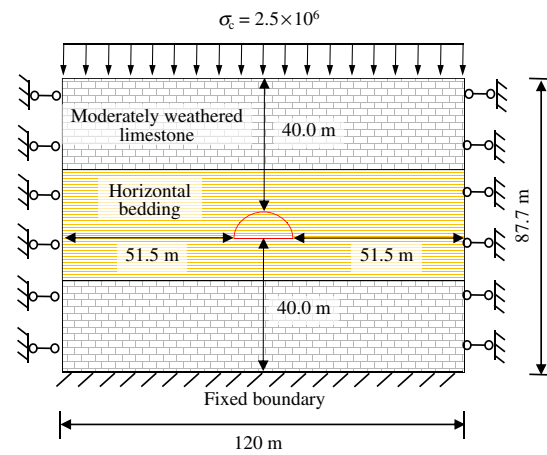
Combining Eq. (4) and Eq. (5), the deformations of the total joint planes $d\varepsilon^J$ can be found as

$$d\varepsilon^J = \frac{1}{d} \mathbf{B}^T \mathbf{L}^T \mathbf{DLB} d\sigma \tag{6}$$

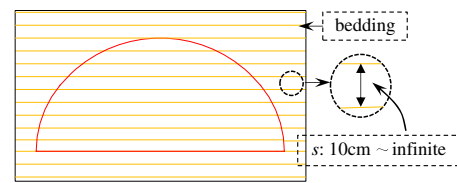
Consequently, the overall average strain of a rock mass can be calculated by Eqs. (1), (2), and (6).

Constitutive model and yield criterion

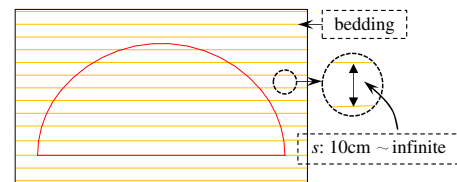
The constitutive model used here is the anisotropic elastoplastic ubiquitous joint model, where a three-dimensional ubiquitous joint analysis has been described and applied to tunnel engineering (Sainsbury and Sainsbury 2017; Das et al. 2017). The ubiquitous joint model is actually an extension of the Mohr-Coulomb constitutive model, which contains joint weak plane in the special



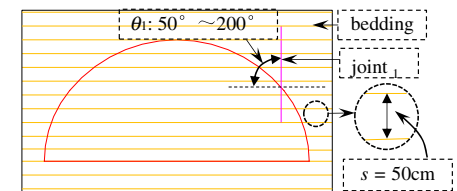
(a)



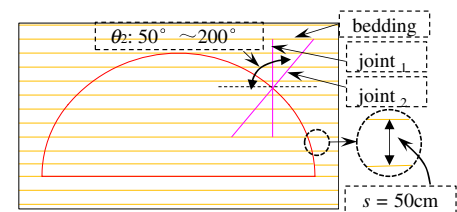
(b)



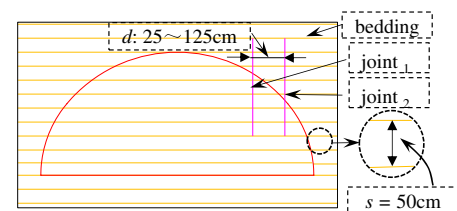
(c)



(d)



(e)



(f)

Fig. 5 Five series of numerical simulations. **a** Numerical model. **b** Series-1: The roof of tunnel is located on a bedding plane. **c** Series-2: The roof of tunnel is located inside rock masses between two bedding planes. **d** Series-3: $s = 50$ cm and considering θ_1 changed from 50° to 200° . **e** Series-4: $s = 50$ cm and $\theta_1 = 90^\circ$ and considering θ_2 changed from 50° to 200° . **f** Series-5: $s = 50$ cm and $\theta_1 = \theta_2 = 90^\circ$ considering d changed from 25 to 125 cm

direction. The failure criterion of joint weak plane used here is the Mohr-Coulomb yield criterion with tension cutoff as defined in Eqs. (7) and (8).

$$f_j^s = \sigma_3 - \sigma_1 + (\sigma_3 + \sigma_1)\sin\phi_j - 2c_j\cos\phi_j = 0 \tag{7}$$

$$f_j^t = \sigma_3 - \sigma_j^t = 0 \tag{8}$$

where φ_j is friction angle; c_j is cohesion; σ_j^t is tensile strength.

The plastic shear potential corresponds to a non-associated flow rule by using dilation angle ψ_j instead of φ_j (Eq. (9)), while the tensile plastic potential follows an associated flow rule (Eq. (10)). The implicit functions g_s and g_t are used to characterize the shear and tensile plastic flow laws of materials.

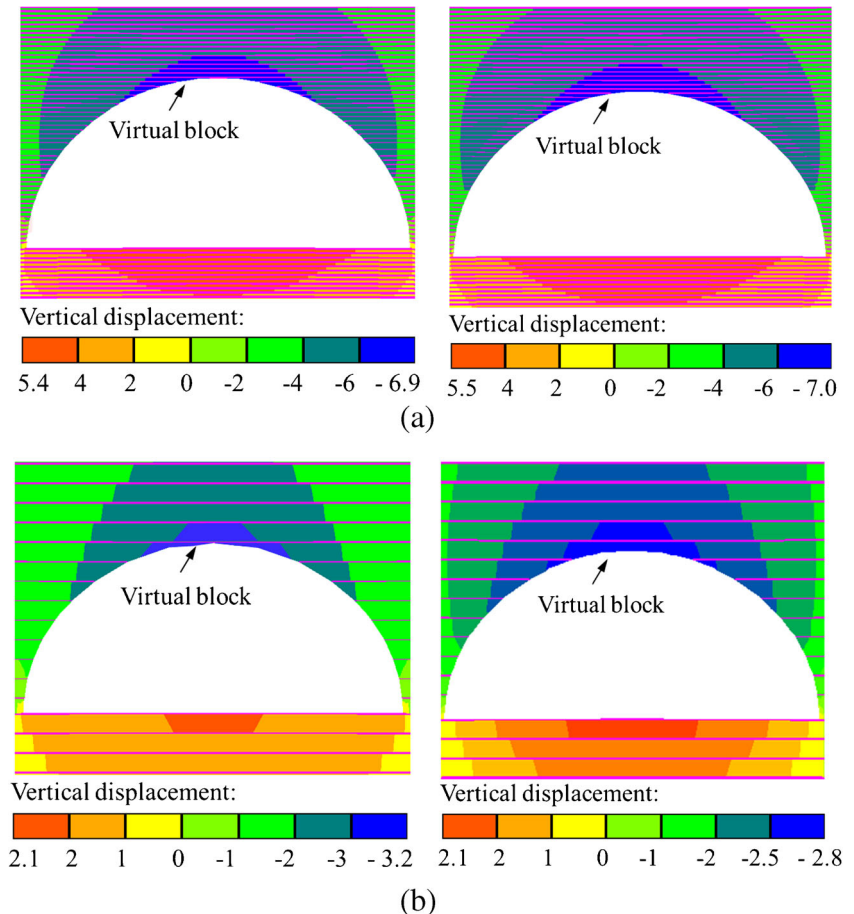
$$g_s = \sigma_3 - \sigma_1 + (\sigma_3 + \sigma_1)\sin\psi_j = const. \tag{9}$$

$$g_t = \sigma_3 \tag{10}$$

Table 1 Material properties used in numerical analysis

Structural components	Bulk density (kN/m ³)	Young's modulus (GPa)	Poisson's ratio	Cohesion (MPa)	Friction angle (°)	Tensile strength (MPa)
Moderately weathered limestone	25	6.7	0.28	1.3	32	1.0
Bedding plane	–	–	–	0.2	30	0.1
Joint plane	–	–	–	0.1	26	0.1

Fig. 6 Vertical deformations and failure modes of the stratified surrounding rock masses (without joint) in the series-1 and series-2 tests with different s (unit: cm). **a** $s = 10$ cm. **b** $s = 90$ cm



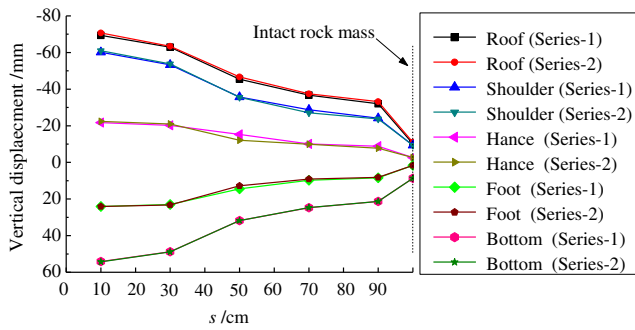


Fig. 7 Vertical displacements of key points surrounding a tunnel with various *s*

Model implementation

The incremental numerical algorithm, whose main task is to compute new stresses from strain increments, is described by the following steps. First, it is necessary to determine whether the surrounding rock masses enter the failure state. Then, the rock stresses iteratively by applying the corresponding correction rules are calculated. Finally, the updated stress is analyzed. When the surrounding rock masses are in a stable stress state (elastic state), no plastic correction is required. When the surrounding rock masses are in a yield state, it needs to be modified according to the correlation (non-correlation) flow rule.

Issues related to tunnel in jointed rock masses under excavation

Engineering situation and surrounding rock characteristics

The Panlongshan tunnel in Shandong Province, China, is located in the northwest edge of the Mount Tai. The length of the left tunnel is 2885 m and the mileage is from ZK78 + 345 to ZK81 + 230. The length of the right tunnel is 2875 m and the mileage is from YK78 + 345 to YK81 + 220. The maximum depth of the tunnel is 160 m. The longitudinal geological profile of the tunnel is shown in Fig. 2 a. The tunnel is a two-way separation-type tunnel with six lanes. The net width and height of the standard section of the V rock is 17.84 m and

12.70 m, respectively (Fig. 2b). The rock masses surrounding the tunnel are moderately weathered limestone, offwhite, bedding, and joint structures.

The sections of ZK80 + 206~ZK80 + 267 are investigated. Figure 3 shows the bedding and joint characteristics and typical failure modes of test sections after tunnel excavation. It can be found that the surrounding rock masses around the tunnel are fragmented. The spacing of bedding is different which ranges from several to tens of centimeters. The rock masses in the roof and shoulders of the tunnel are prone to falling off, and a severe overbreak occurs on these positions, namely, (a) roof falling, which mainly manifests in roof rock masses separating from bedding planes and resembling a “doorframe” (Fig. 3a); (b) stepped rock masses, which the rock masses in the shoulders drop along joint planes and form stepped distributions. The maximum stepped height and width of surrounding rock masses at the shoulder position are 72 cm and 34 cm, respectively (Fig. 3b and c).

Tunnel overbreak

The Panlongshan tunnel is constructed by bench dynamic excavation method. The designed width, height, and area of the upper bench are 17.0 m, 7.5 m, and 103.8 m², respectively. Based on the experience of tunnel blasting excavation and field investigation, overbreak will inevitably occur in the excavation of the tunnel upper bench. This will lead to the difficulty in steel arch erection, the waste of shotcrete, and the instability of the surrounding rock masses. To quantify the overbreak area of the upper bench, several cross-sectional areas of the tunnel were measured. Figure 4 presents the measurement results of two serious overbreak sections. The maximum linear overbreak is 39.0 cm and 35.2 cm in the roof, 82.5 cm and 80.1 cm in the left arch shoulder, and 81.2 cm and 75.3 cm in the right arch shoulder. The overbreak areas of the two sections are 13.17 m² and 11.16 m², accounting for 12.7% and 10.8% of the tunnel upper bench area, respectively.

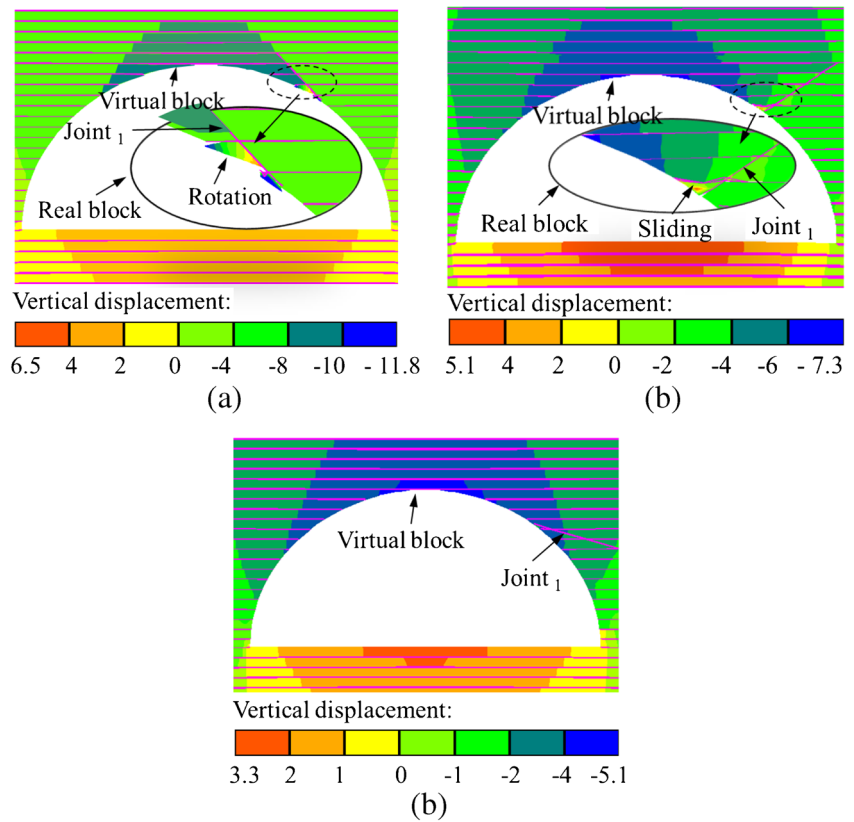
Numerical model

To provide an insight into the deformation mechanisms and failure modes of tunnels in jointed rock masses, a series of numerical

Table 2 Failure zone volumes of the tunnel surrounding rock masses with various *s*

Failure zone volume/m ³	Measured results		Numerical results						
	ZK80+250.4	ZK80+246.5	Series-1	Series-2	10 cm	30 cm	50 cm	70 cm	90 cm
52.7		44.6	65.2	49.8	38.6	22.4	14.3		
			73.6	57.3	45.5	28.6	20.2		

Fig. 8 Vertical deformations and failure modes of the jointed surrounding rock masses in the series-3 tests (with one joint) with various θ_1 (unit: cm). **a** $\theta_1 = 50^\circ$. **b** $\theta_1 = 150^\circ$. **c** $\theta_1 = 200^\circ$



analysis was performed by using FLAC3D, and the anisotropic elastoplastic ubiquitous joint model was adopted.

Five series of numerical simulations were conducted by considering the influences of beddings, joints, and cross cutting between them (Fig. 5). The numerical model is 120 m in width, 87.7 m in height, and 4.0 m (the length of one excavation) in longitudinal length. There are usually two methods to simulate the weak plane of jointed rock masses in numerical simulation: the weak intercalated layer method and zero-

thickness contact element method (Goodman 1976; Mei 2008). The two simulation methods have little difference as long as the strength of the weak plane is consistent. In this paper, the zero-thickness contact element method is adopted to simulate the bedding and joint planes. Based on the geological exploration data and geotechnical tests, contact normal stiffnesses of 2.5×10^9 Pa/m and 1.2×10^9 Pa/m and contact shear stiffnesses of 1.0×10^9 Pa/m and 0.8×10^9 Pa/m are used to represent deformability of the bedding and joint planes, respectively. The other mechanical parameters of the moderately weathered limestone and the bedding and joint planes are listed in Table 1.

As shown in Figs. 5 b and c, the series-1 and series-2 tests contain eleven models with different s , which are set to $s = 10$ cm, 30 cm, 50 cm, 70 cm, 90 cm, and infinite, respectively. In the series-1 tests, the roof of tunnel is tangent to the bedding plane, and in the series-2 tests, the roof is located in the middle of two bedding planes. The series-3, series-4, and series-5 tests aim at discussing the effect of joint planes on the mechanical behaviors of the jointed rock masses. The influence of θ_1 and θ_2 and d are discussed in Figs. 5 d, e, and f. In the series-3 and series-4 tests, θ_1 and θ_2 are set to $50^\circ, 70^\circ, 90^\circ, 110^\circ, 130^\circ, 150^\circ,$ and 200° , respectively. Meanwhile, d is set to 25 cm, 50 cm, 75 cm, 100 cm, and 125 cm in the series-5 tests, respectively.

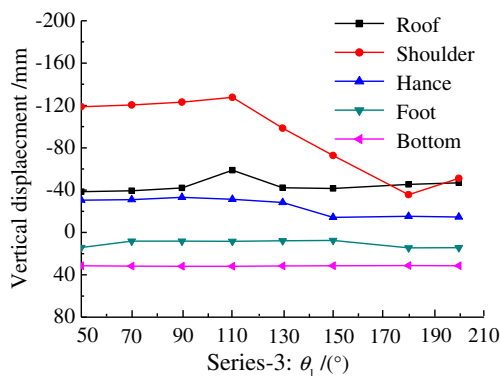
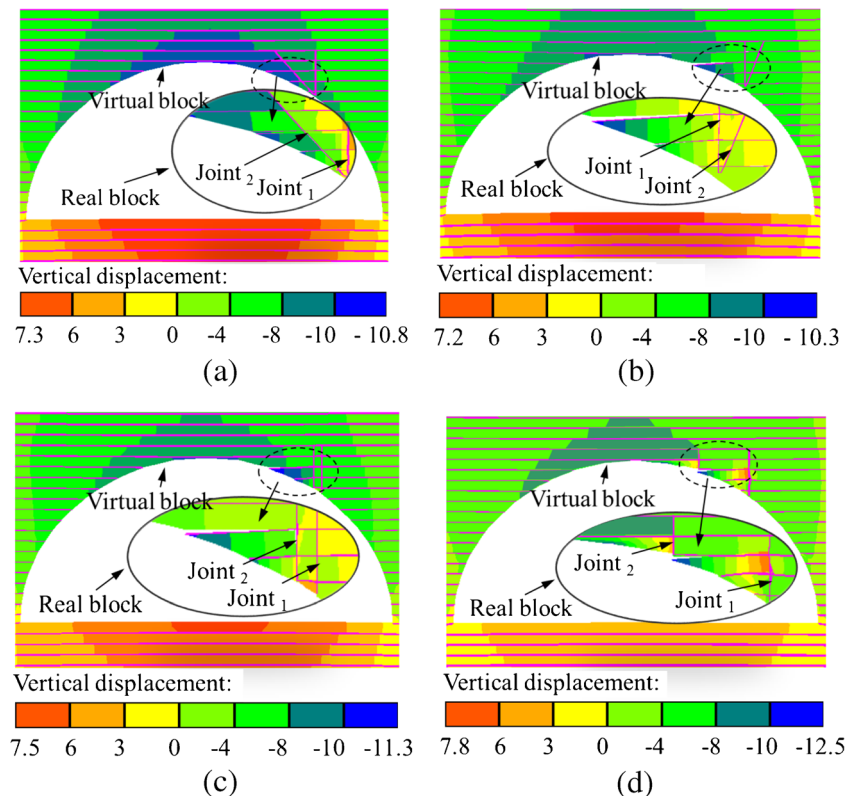


Fig. 9 Vertical displacements of key points surrounding a tunnel with different θ_1

Fig. 10 Vertical deformations and failure modes of the jointed surrounding rock masses in the series-4 and series-5 tests (with two joints) with different θ_2 or d (unit: m). **a** $\theta_2 = 50^\circ$. **b** $\theta_2 = 110^\circ$. **c** $d = 25$ cm. **d** $d = 125$ cm



Results and discussion

Deformations and failure modes of tunnel surrounding rock masses

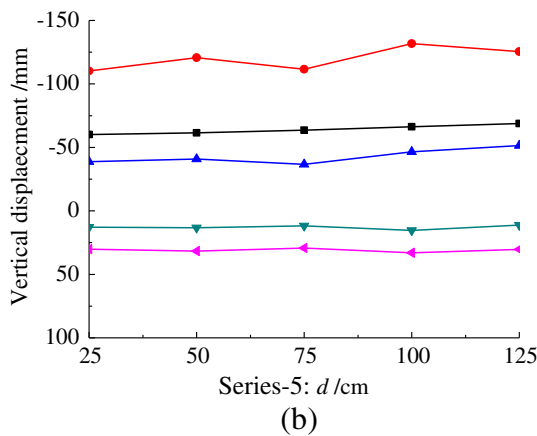
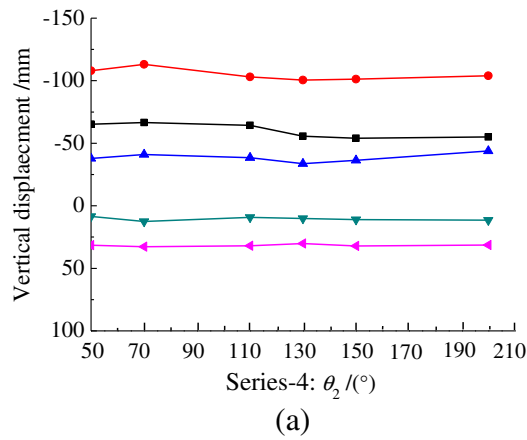
Effects of s

Figure 6 shows the vertical deformations and failure modes of the stratified surrounding rock masses (without joint) in the series-1 and series-2 tests with different s . For the convenience of our statement, two representative models ($s = 10$ cm and $s = 90$ cm) are shown in Fig. 6. Figure 7 presents the vertical displacements of key points surrounding a tunnel with various s . With the increase in s , the vertical deformation of surrounding rock masses gradually decreases. The maximum settlement surrounding the tunnel is located at the roof. As s changes from 10 cm to infinite (intact rock mass), the maximum settlement decreases from -70.4 to -10.2 mm. This indicates that the bedding structure plays a vital role on the vertical deformation of surrounding rock masses after tunnel excavation. The smaller the value of s , the greater the discontinuity and the more broken the rock masses, and the larger the deformation of the surrounding rock after the tunnel excavation.

Table 2 summarizes the sizes of failure zone volume with different s after tunnel excavation. The measured results are

obtained by the overbreak area multiplied by the length of one excavation (4.0 m). The shear-now and tension-now failure elements are taken into consideration in the numerical results, which indicate the elements have entered shear failure or tensile failure during the current calculation step. It can be drawn from Fig. 6 and Table 2, some “virtual blocks” are formed in the roof of tunnel, which constitute the main part of the unstable areas. The spacing of discontinuities determines the sizes of the blocks making up the stratified surrounding rock masses. The values of failure zone volume increase significantly with the decrease in s . The separation of “virtual blocks” along the bedding planes is a basic failure mode. The numerical results are in good agreement with Zhang et al.’s research results (Zhang et al. 2012).

Figure 7 shows there is little difference on the vertical displacements of key points surrounding the tunnel when the roof is located on a bedding plane or inside rock masses. However, as listed in Table 2, the failure zone volumes seem relatively bulky for the series-2 compared with that of the series-1 and the maximal difference is 8.5 m³. This indicates that when the tunnel roof is located inside the rock masses, the rock masses nearby the roof are easier to be destroyed along the adjacent bedding plane during tunnel excavation. Furthermore, based on comparison analysis between the measured results and the series-1 and series-2 numerical results, the height of “virtual block” of the stratified



—■— Roof —●— Shoulder —▲— Hance —▼— Foot —▲— Bottom

Fig. 11 Vertical displacement distributions of the tunnel with different θ_2 or d . **a** Series-4: $\theta_2 = 50^\circ\sim 200^\circ$. **b** Series-5: $d = 25\sim 125$ cm

surrounding rock masses is mainly from 10 to 70 cm. This is in agreement with the measured results of the failure height of the tunnel roof and shoulder rock masses in Fig. 3.

Effects of θ_1

Figure 8 shows the vertical deformations and failure modes of the jointed surrounding rock masses in the series-3 tests (with one joint in the right arch shoulder) with various θ_1 , and only

three representative models ($\theta_1 = 50^\circ$, $\theta_1 = 150^\circ$, and $\theta_1 = 200^\circ$) are shown in Fig. 8. Figure 9 presents the vertical displacements of key points surrounding a tunnel with different θ_1 . The joint has a great influence on the vertical deformations of surrounding rock masses after tunnel excavation, and the maximum vertical displacement of the tunnel appears in the joint position rather than the roof. As θ_1 varies from 50° to 200° , the maximum settlement at the joint position increases from -118.2 to -127.6 mm then decreases to -51.2 mm.

With respect to the series-3 tests, after excavation, the failure mode is predominantly controlled by the structure of the jointed rock mass. In the joint position, some “real blocks” compose unstable rock masses, which are formed by common cuttings of the tunnel outline, bedding planes, and joint plane. When θ_1 changes from 50° to 150° , these “real blocks” are broken. After excavation, the bedding and joint planes close to these “real blocks” have been separated resulting from excavation disturbance and their own gravity. Then, these “real blocks” are easy to slip, rotate, and fall down along the joint dip, resulting in overbreak. The rotation of “real blocks” happens when θ_1 ranges from 50° to 90° (Fig. 8a). The sliding of “real blocks” can take place when $\theta_1 = 90^\circ\sim 150^\circ$ (Fig. 8b). In the case of $\theta_1 = 180^\circ$, the joint plane overlaps the bedding plane. The failure mode of surrounding rock masses is attributed to “virtual blocks.” Besides, it is observable in Fig. 8 c that in the case of $\theta_1 = 200^\circ$, no complete failure of the “real blocks” has occurred. These “real blocks” only have certain deformation and the surrounding rock masses are still relatively stable. This may be because the bond strength and friction between contact surfaces of these “real blocks” can restrain the influence of excavation disturbance and gravity.

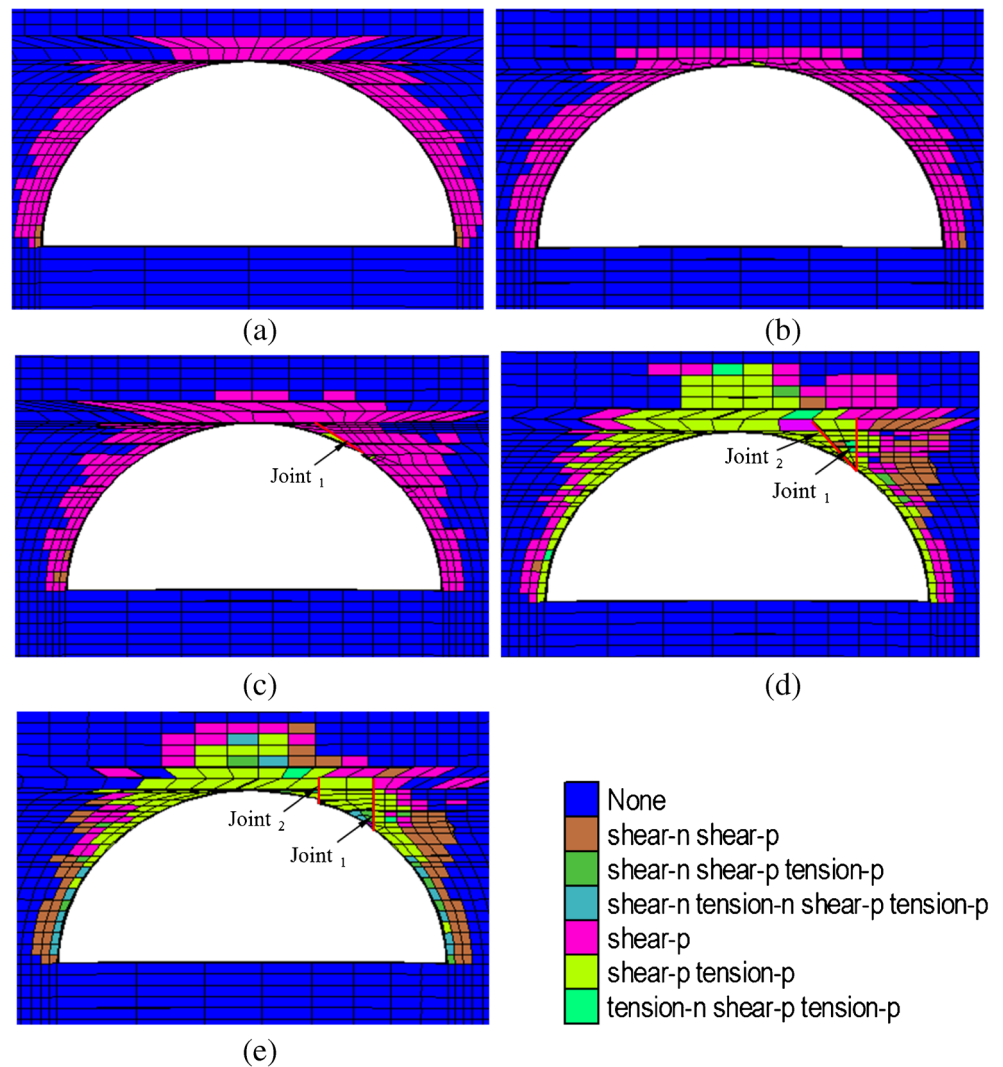
Effects of θ_1 , θ_2 , and d

Figure 10 shows the vertical deformations and failure modes of the surrounding rock masses in the series-4 and series-5 tests (with two joints in the right arch shoulder). For the convenience of our statement, only four representative models are shown in Fig. 10, in which $\theta_2 = 50^\circ$ and $\theta_2 = 110^\circ$ or $d = 25$ cm and $d = 125$ cm. Figure 11 presents the vertical displacements of key points surrounding a tunnel. The maximum vertical

Table 3 Failure zone volumes of surrounding rock masses with different θ or d

Failure zone volume/m ³	Series-3							
	50°	70°	90°	110°	130°	150°	180°	200°
	49.7	52.3	53.8	55.3	48.2	41.3	38.6	40.8
Series-4	50°	70°	110°	130°	150°	200°		
	53.2	55.6	59.4	58.3	52.1	50.7		
Series-5	25 cm	50 cm	75 cm	100 cm	125 cm			
	55.1	54.5	57.2	58.6	59.7			

Fig. 12 Plastic zone distributions of the jointed surrounding rock masses after tunnel excavation, here $s = 50$ cm. **a** Series-1. **b** Series-2. **c** Series-3, where $\theta_1 = 50^\circ$. **d** Series-4, where $\theta_1 = 90^\circ$ and $\theta_2 = 50^\circ$. **e** Series-5, where $\theta_1 = \theta_2 = 90^\circ$ and $d = 125$ cm



deformation of the tunnel is still located in the joint position. When θ_2 changes from 50° to 200° or d varies from 25 to 125 cm, the maximum settlement of the joint position fluctuates at about 110 mm. The maximum settlement of the joint position is about 2 times than that value of the roof. The settlements of the roof are about 15 mm larger than that in the series-3 tests.

It is clear that more “real blocks” are formed by common cuttings of the tunnel outline, bedding planes, and two joint planes, resulting in very large failure zones. Table 3 summarizes the sizes of failure zone volume of the surrounding rock masses for the series-3, series-4, and series-5 tests after tunnel excavation. Apparently, the number of joints has a significant effect on the size of failure zone volume. Compared with the case of one joint, the increment of the maximum value of failure zone volume is 4.4 m^3 . Further comparison with the case of no joint (see Table 2, where $s = 50$ cm), the increment of the maximum value of failure zone volume is 14.2 m^3 . So the results indicate that after excavation, the more complex the joint structures in jointed rock masses are, the more unstable rock masses are formed.

Plastic zone distributions of tunnel surrounding rock masses

Figure 12 exhibits the plastic zone distributions of the surrounding rock masses ($s = 50$ cm) after tunnel excavation. Where none is elastic zones; shear-p and tension-p are shear and tension plastic zones in the past calculation step, respectively; shear-n and tension-n are shear and tension plastic zones in the current calculation step, respectively. The results show that the number and state of joints have prominent effects on the distributions of plastic zone of the jointed rock masses, and the shape as well as extent of the plastic zone is also strongly dependent on the dip angle. As illustrated in Fig. 12, we can see that for the stratified surrounding rock masses (without joint), the plastic zone distribution around tunnel is symmetric. But for jointed rock mass, with the introduction of joint, the distribution of plastic zone becomes asymmetric; the plastic zone areas in the joint positions are obviously large. Moreover, with the increase of the number of joints in the right

shoulder, the plastic zone at this position has a developing tendency towards the deep part, and the area of plastic zone at the roof and right arch shoulder tends to increase. These can be used to explain the above conclusion: the more complex the joint structures in jointed rock masses are, the more unstable rock masses are formed.

Conclusions

This paper presented a field survey of failure modes and overbreak of the Panlongshan tunnel and a corresponding 3D numerical simulation analysis on the failure modes of the tunnel in jointed rock masses. The field survey and numerical analysis indicate that the bedding and joint structures and the joint dip angle have significant influences on the deformations and the failure mechanisms of tunnel after excavation. The following conclusions are drawn:

After tunnel excavation, the vertical deformations of the stratified surrounding rock masses (without joint) gradually decrease with the increase in s , and the maximum settlement around the tunnel is located at the roof. However, for the stratified rock masses containing joints, the maximum vertical deformation of the tunnel appears in the joint position. The maximum settlement of the joint position is about 2 times than that value of the roof.

This paper introduces the “virtual blocks” and “real blocks” concepts for the analysis of failure zones of jointed rock masses. For the stratified rock masses, the smaller the s is, the larger the volume of failure zone tends to be. For the stratified rock masses containing one joint, the rotation of “real blocks” happens when θ_1 ranges from 50° to 90° , and the sliding of “real blocks” can take place when $\theta_1 = 90^\circ$ – 150° . For the stratified rock masses containing two joints, more “real blocks” are formed, resulting in a larger failure zone. It is suggested to consider the dimension and failure modes of the “virtual blocks” and “real blocks” in designing rock support systems for the jointed rock masses.

The plastic zone distributions of the jointed surrounding rock masses are also discussed in this paper. With the increase of the number of joints, the plastic zone at the joint positions has a developing tendency towards the deep part. As a result, there are more unstable rock masses formed. It is helpful to deepen our understanding on the failure mechanisms of jointed rock masses due to excavation.

Authors' contributions B.X. (Bangshu Xu), W.Z. (Wanzhi Zhang), G.Y. (Guangyao Yue), and W.S. (Weihang Shi) carried out the field monitoring and obtained the overbreak data; W.Z. and J.M. (Jie Mei) performed the numerical experiments and wrote the original manuscript; B.X. reviewed and revised the original manuscript.

Funding information This research was supported by the National Nature Science Foundation of People's Republic of China (Grant No. 50909056).

Compliance with ethical standards

Conflict of interest The authors declare that they have no conflict of interest.

References

- Wu B (2016) Study on disturbance zone evolution and anchoring mechanism of surrounding rock in layered rock tunnel. China University of Geosciences, Wuhan, China, Doctoral dissertation (in Chinese)
- Lisjak A, Grasselli G, Vietor T (2014) Continuum–discontinuum analysis of failure mechanisms around unsupported circular excavations in anisotropic clay shales. *International Journal of Rock Mechanics and Mining Sciences*. 65(19):96–115
- Zhang Y, Liu Y (2002) Three-dimensional elastic-plastic finite element analysis of stratified rock. *Chinese Journal of Rock Mechanics and Engineering*. 21(11):1615–1619 (in Chinese)
- Goodman RE (1989) Introduction to rock mechanics, second ed. John Wiley and Sons, New York, 1989.
- Wu JH, Ohnishi Y, Nishiyama S (2004) Simulation of the mechanical behavior of inclined jointed rock masses during tunnel construction using discontinuous deformation analysis (DDA). *International Journal of Rock Mechanics and Mining Sciences*. 41(5):731–743
- Huang X, Zhang Z (2012) Stress arch bunch and its formation mechanism in blocky stratified rock masses. *Journal of Rock Mechanics and Geotechnical Engineering*. 4(1):19–27
- Stille H, Palmstrom A (2008) Ground behaviour and rock mass composition in underground excavations. *Tunnelling Underground Space Technology*. 23(1):46–64
- Zheng Y, Wang Y, Wang C et al (2011) Stability analysis and exploration of failure law of jointed rock tunnel—seminor on tunnel stability analysis. *Chinese Journal of Underground Space and Engineering*. 7(4):649–656 (in Chinese)
- Wang P, Cai M, Ren F (2018) Anisotropy and directionality of tensile behaviours of a jointed rock mass subjected to numerical Brazilian tests. *Tunnelling and Underground Space Technology*. 73:139–153
- Evans WH (1941) The strength of undermined strata. *Trans. Inst. Min. Metall.* 50:475–500
- Beer G, Meek JL (1982) Design curves for roofs and hanging-walls in bedded rock based on ‘voussoir’ beam and plate solutions. *Trans. Inst. Min. Metall.* 91:A18–A22
- Xiao Y, Ding E (1993) Study on the stability of the jointed roof. *Chinese Journal of Rock Mechanics and Engineering*. 12(4):353–365 (in Chinese)
- Diederichs MS, Kaiser PK (1999) Stability of large excavations in laminated hard rock masses: the voussoir analogue revisited. *International Journal of Rock Mechanics and Mining Sciences*. 36(1):97–117
- Yang J, Yang W, Guo Y (2001) Analysis of buckling failure of layered roof of coal roadway. *Journal of China Coal Society*. 26(3):240–244 (in Chinese)
- Huang N, Liu R, Jiang Y, Cheng Y, Li B (2019) Shear-flow coupling characteristics of a three-dimensional discrete fracture network-fault model considering stress-induced aperture variations. *Journal of Hydrology* 571:416–424
- Hao YH, Azzam R (2005) The plastic zones and displacements around underground openings in rock masses containing a fault. *Tunnelling and Underground Space Technology incorporating Trenchless Technology Research*. 20(1):49–61

- Jiang Y, Tanabashi Y, Li B, Xiao J (2006) Influence of geometrical distribution of rock joints on deformational behavior of underground opening. *Tunnelling and Underground Space Technology*. 21(5): 485–491
- Jia P, Tang CA (2008) Numerical study on failure mechanism of tunnel in jointed rock mass. *Tunnelling & Underground Space Technology Incorporating Trenchless Technology Research* 223(5):500–507
- Jeon S, Kim J, Seo Y, Hong C (2004) Effect of a fault and weak plane on the stability of a tunnel in rock – a scaled model test and numerical analysis. *International Journal of Rock Mechanics and Mining Science*. 41(1):658–663
- Liu X, Chen H, He C (2017) Model test and stress distribution law of unsymmetrical loading tunnel in bedding rock mass. *Arabian Journal of Geosciences*. 10(7):184
- Chen X, Liao Z, Peng X (2013) Cracking process of rock mass models under uniaxial compression. *J. Cent. South Univ*. 20:1661–1678
- Bahaaddini M, Sharrock G, Hebblewhite B (2013) Numerical investigation of the effect of joint geometrical parameters on the mechanical properties of a non-persistent jointed rock mass under uniaxial compression. *Comput. Geotech*. 49:206–225
- Han G, Jing H, Jiang Y, Liu R, Su H, Wu J (2018) The effect of joint dip angle on the mechanical behavior of infilled jointed rock masses under uniaxial and biaxial compressions. *Processes*. 6:49
- Jaeger JC, Cook N (1979) *Fundamentals of rock mechanics*. third edition. Science Paperbacks. 9(3):251–252(2)
- Prudencio M, Jan MVS (2007) Strength and failure modes of rock mass models with non-persistent joints. *International Journal of Rock Mechanics and Mining Sciences*. 44(6):890–902
- Zhang ZX, Xu Y, Kulatilake PHSW, Huang X (2012) Physical model test and numerical analysis on the behavior of stratified rock masses during underground excavation. *International Journal of Rock Mechanics and Mining Sciences*. 49:134–147
- Song JJ, Lee CI, Seto M (2001) Stability analysis of rock blocks around a tunnel using a statistical joint modeling technique [J]. *Tunnelling and Underground Space Technology*. 16(4):341–351
- Itasca Consulting Group, Inc. (2012) *FLAC3D (Fast Lagrangian Analysis of Continua in Three-dimensions)*, version 5.0, user's manual. Itasca Consulting Group, Inc.
- Yang ZM, Wu SC, Gao YT, Jin AB, Cong ZJ (2018) Time and technique of rehabilitation for large deformation of tunnels in jointed rock masses based on FDM and DEM numerical modeling. *Tunnelling and Underground Space Technology*. 81:669–681
- Wang TT, Huang TH (2009) A constitutive model for the deformation of a rock mass containing sets of ubiquitous joints. *International Journal of Rock Mechanics and Mining Sciences*. 46(3):521–530
- Sainsbury BL, Sainsbury DP (2017) Practical use of the ubiquitous-joint constitutive model for the simulation of anisotropic rock masses. *Rock Mechanics and Rock Engineering*. 50:1–22
- Das AJ, Mandal PK, Bhattacharjee R, Tiwari S, Kushwaha A, Roy LB (2017) Evaluation of stability of underground workings for exploitation of an inclined coal seam by the ubiquitous joint model. *International Journal of Rock Mechanics and Mining Sciences*. 93: 101–114
- Goodman RE (1976) *Methods of geological engineering in discontinuous rocks*. West Pub, Co
- Mei S (2008) Study on deformation mechanism and failure characteristics of layered rock masses due to excavation. Doctoral dissertation. Wuhan Institute of Rock and Soil Mechanics. The Chinese Academy of Science, P. R. China. (in Chinese).